frontiers in Earth Science

ORIGINAL RESEARCH
published: 24 September 2018
doi: 10.3389/feart.2018.00141

Seismicity Associated With the Formation of a New Island in the Southern Red Sea

Jade H. W. Eyles[1,2], Finnigan Illsley-Kemp[1,3], Derek Keir[1,4], Joël Ruch[5,6] and Sigurjón Jónsson[6]*

[1] Ocean and Earth Science, University of Southampton, Southampton, United Kingdom, [2] School of Environmental Sciences, University of East Anglia, Norwich, United Kingdom, [3] School of Geography, Environment and Earth Sciences, Victoria University of Wellington, Wellington, New Zealand, [4] Dipartimento di Scienze della Terra, Universita degli Studi di Firenze, Florence, Italy, [5] Department of Earth Sciences, University of Geneva, Geneva, Switzerland, [6] Physical Science and Engineering Division, King Abdullah University of Science and Technology, Thuwal, Saudi Arabia

Volcanic eruptions at mid-ocean ridges are rarely witnessed due to their inaccessibility, and are therefore poorly understood. Shallow waters in the Red Sea allow the study of ocean ridge related volcanism observed close to sea level. On the 18th December 2011, Yemeni fishermen witnessed a volcanic eruption in the Southern Red Sea that led to the formation of Sholan Island. Previous research efforts to constrain the dynamics of the intrusion and subsequent eruption relied primarily on interferometric synthetic aperture radar (InSAR) methods, data for which were relatively sparse. Our study integrates InSAR analysis with seismic data from Eritrea, Yemen, and Saudi Arabia to provide additional insights into the transport of magma in the crust that fed the eruption. Twenty-three earthquakes of magnitude 2.1–3.9 were located using the Oct-tree sampling algorithm. The earthquakes propagated southeastward from near Sholan Island, mainly between December 12th and December 13th. The seismicity is interpreted as being induced by emplacement of a ∼12 km-long dike. Earthquake focal mechanisms are primarily normal faulting and suggest the seismicity was caused through a combination of dike propagation and inflation. We combine these observations with new deformation modeling to constrain the location and orientation of the dike. The best-fit dike orientation that satisfies both geodetic and seismic data is NNW-SSE, parallel to the overall strike of the Red Sea. Further, the timing of the seismicity suggests the volcanic activity began as a submarine eruption on the 13th December, which became a subaerial eruption on the 18th December when the island emerged from the beneath the sea. The new intrusion and eruption along the ridge suggests seafloor spreading is active in this region.

Keywords: Red Sea, mid-ocean ridge, dike, seismicity, InSAR, eruption

OPEN ACCESS

Edited by:
Benoit Taisne, Nanyang Technological University, Singapore

Reviewed by:
Luca De Siena, University of Aberdeen, United Kingdom
Eisuke Fujita, National Research Institute for Earth Science and Disaster Prevention, Japan

***Correspondence:**
Derek Keir
d.keir@soton.ac.uk

Specialty section:
This article was submitted to Volcanology, a section of the journal Frontiers in Earth Science

Received: *04 June 2018*
Accepted: *05 September 2018*
Published: *24 September 2018*

Citation:
Eyles JHW, Illsley-Kemp F, Keir D, Ruch J and Jónsson S (2018) Seismicity Associated With the Formation of a New Island in the Southern Red Sea. Front. Earth Sci. 6:141. doi: 10.3389/feart.2018.00141

INTRODUCTION

Magma motion through the crust can induce earthquakes, the analysis of which is a useful tool to understand when, where, and how magma is transported. The understanding of magma intrusion and volcanism is key for understanding dynamic processes that occur at divergent boundaries (e.g., Ebinger et al., 2013; Pagli et al., 2015; Ruch et al., 2016; Wilcock et al., 2016). However,

the understanding of the extensional processes at submarine ocean ridges in space and time is limited by the difficulty associated with observing seismicity and ground deformation in the deep oceans (e.g., Soule et al., 2007; Carey et al., 2018). Over the past 20 years, the Southern Red Sea has experienced six seismic swarms interpreted to be related to magma intrusions (Xu et al., 2015). The Southern Red Sea has a large proportion of shallow waters, which provide a rare opportunity to study volcanic eruptions that occur above sea level (**Figure 1**). Three sub-aerial volcanic eruptions have occurred in the last decade: on Jebel at Tair island (2007) and two eruptions resulting in the formation of Sholan Island (2011) and Jadid Island (2013) (Jónsson and Xu, 2015). All the islands lie on the rift axis of the Southern Red Sea. The eruptions of Jebel at Tair and Jadid lasted 8 and 2 months, respectively, and followed short duration (days) low magnitude ($M > 4$) seismic swarms thought to be caused by the intrusion of magma through the crust to the Earth's surface (Xu et al., 2015). The eruption of Jebel at Tair was subaerial, while the first half of the Jadid eruption was submarine (Xu et al., 2015).

The eruption of Sholan Island occurred between Haycock and Rugged islands in the Zubair Archipelago and was first witnessed by Yemeni fishermen on the 18th December 2011 (**Figure 2**). The eruption started as submarine activity before erupting as a surtseyan eruption, and lasted until the 12th January 2012 (Jónsson and Xu, 2015). A SO_2 anomaly was first recorded on the 19th December from the Ozone Monitoring Instrument (OMI) taken on NASA's EOS-AURA satellite; maximum SO_2 values reached 2.06 DU. The newly formed island joined ten pre-existing volcanic islands known as the Zubair Archipelago (**Figure 2**); the island consisted primarily of hydromagmatic deposits reaching a maximum of 0.25 km^2 (Xu et al., 2015). The Sholan eruption was soon followed by the eruption and formation of Jadid Island in September 2013, situated between Saddle and Saba Islands (**Figure 2**). The eruption at Jadid lasted for 54 days and the island reached a maximum size of $\sim$0.68 km^2 (Xu et al., 2015). Optical imagery taken from the Sentinel-2 satellites shows that Sholan and Jadid island are still visible today.

Xu et al. (2015) used interferometric synthetic aperture radar (InSAR) to measure centimeter-scale ground deformation during the eruption of Sholan and Jadid islands, and modeled dikes to account for the observed deformation. For the Sholan eruption one interferogram from 13th October 2011 to the 15th December 2012 was used for interpretation; 1.5 and 3 cm of deformation were observed on Saba and Zubair islands, respectively. In addition, optical imagery on the 23rd December 2011 showed the eruption coming from a short N-S fissure as well as a new fracture system orientated NW-SE on Haycock Island (Xu et al., 2015). Accounting for this widespread deformation, Xu et al. (2015) modeled a 1.5 m thick, 10-km-long, north-south orientated feeder dike under Sholan Island responsible for this eruption. For the 2013 Jadid eruption, two interferograms were obtained showing several continuous deformation fringes on Saba and Zubair island; a 1 m thick, 12 km long, NNW-SSE oriented dike was modeled (**Figure 2**).

Preceding the Sholan eruption, three distinct seismic swarms occurred in April, June, and August 2011 and the Yemeni seismological network detected two earthquakes of magnitude 3.7 and 3.9 on the 13th December 2011, taken from the International Seismic Catalogue (ISC). In this study we investigate the temporal and spatial variability in seismic activity prior to the eruption of Sholan Island. Analysis of seismic data from local seismic networks in Eritrea, Yemen, and Saudi Arabia allows us to locate earthquakes surrounding the island which were not recorded by the ISC. The increased number of earthquakes that we detect, coupled with improved relative earthquake locations, allows us to place constraints on the location, timescales and direction of intrusion that fed the eruption. In addition, we use the seismic results to guide new deformation models created from InSAR data. Our data of land-based stations positioned relatively close to an ocean ridge place rare constraints on a seafloor-spreading episode and provide additional insights into the rifting mechanics of the Southern Red Sea.

Tectonic Setting

The Red Sea formed due to the divergence of the Nubian and Arabian plates (Bosworth et al., 2005). Extension and rifting started 25 Ma, the emplacement of dikes throughout the Red Sea begun 24 Ma which was associated with increased volcanism in the region (Bosworth et al., 2005). Rifting of the Red Sea then continued in episodic periods, with seafloor spreading initiating 5 Ma (Bosworth et al., 2005). Magnetic anomalies between 16 and 19^{o}N display five symmetrical magnetic stripes that are interpreted to have begun 3 Ma (Bonatti, 1985; Almalki et al., 2016). Further north, magnetic anomalies become discontinuous before disappearing. This has led some authors to propose that spreading is confined to the Southern Red Sea (Bonatti, 1985), whereas other authors suggest that spreading is evident throughout the Red Sea with the southern end being further evolved (Schettino et al., 2016).

South of 17°N, GPS measurements show the locus of extension splits into two branches: the continuation of the Red Sea ridge in the east, and the Danakil depression to the west (McClusky et al., 2010; **Figure 1**). The bifurcation of the rift into the Danakil depression is thought to have begun 9 Ma (Le Pichon and Gaulier, 1988). The rate of extension increases from 15 mm/year at 16°N to 20 mm/year in the south (13°N), with extension predominantly ENE-WSW (McClusky et al., 2010). GPS velocities show that north of 16^{o}N lateral extension is fully accommodated by the Red Sea ridge, whereas south of 13°N lateral extension is accommodated purely in the Danakil depression (McClusky et al., 2010). Together these account for the total relative plate motion of the Arabian and Nubian plates. The termination of the Southern Red Sea rift is unclear due to conflicted data; bathymetry and gravity data suggests the termination at 14°N, whereas magnetic stripes are only recorded until 15.5°N (Almalki et al., 2016). This suggests a gradual change in spreading from the Red Sea ridge to the Danakil block; extension in the Red Sea ridge decreases to the south, whereas

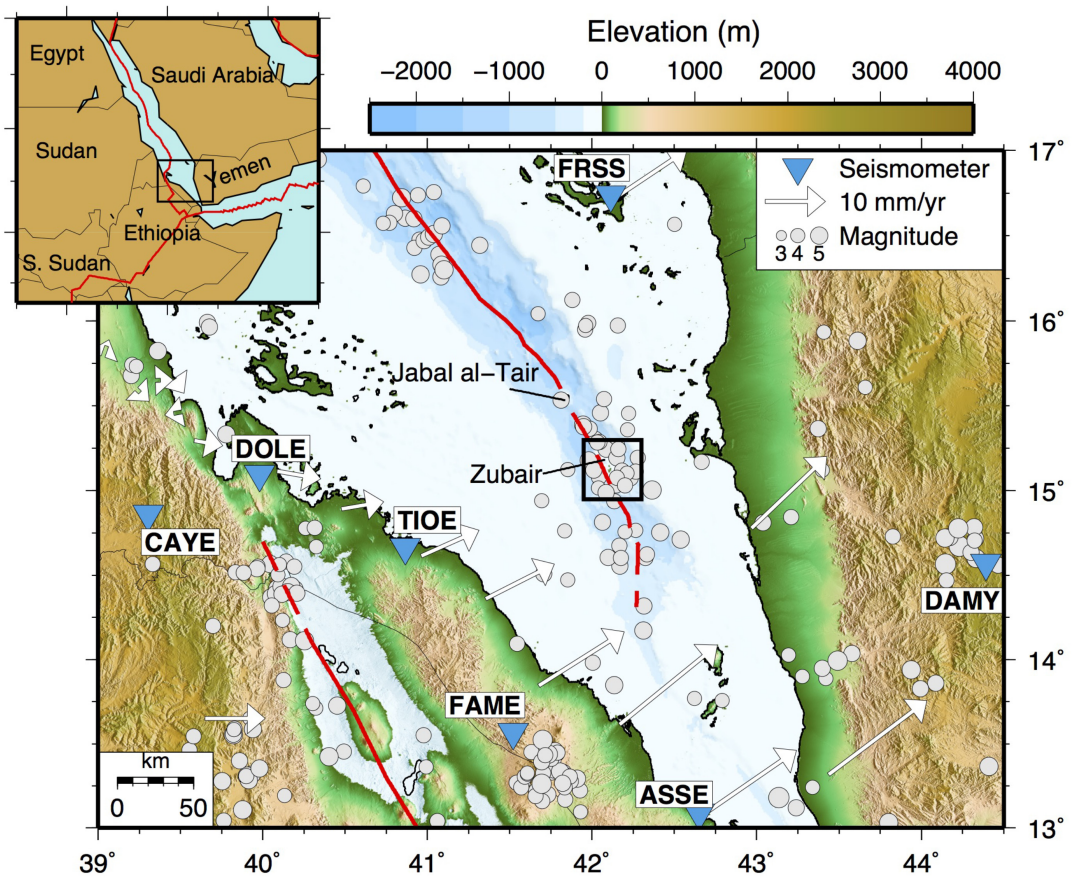

FIGURE 1 | Topographic map of the Southern Red Sea. Gray circles show the NEIC earthquake catalog locations from 1950 to present, red lines denote the axis of extension in the Red Sea and Danakil Depression. GPS measurements taken from McClusky et al. (2010) with respect to the Nubian plate. Black box denotes the Zubair archipelago.

extension gradually increases to the south in the Danakil depression resulting in overlapping ridges in the region 14.5–15.5°N.

The Zubair archipelago (at 15–15.2°N) is a 25 km by 10 km shallow platform [<100 m below sea level (bsl)] orientated parallel to the Red Sea ridge; it consists of ∼10 volcanic islands situated along the central axis of the Red Sea (Jónsson and Xu, 2015). The islands follow a general NW-SE orientation and consist of basaltic tuff, conglomerate, and lava (Jónsson and Xu, 2015). Prior to volcanic activity at the Zubair islands, two known eruptions at Saddle island in 1824 and 1846 are reported, leaving a century of quiescence (Jónsson and Xu, 2015). Over the past few decades the region has seen increased activity. A major rifting event with the intrusion of 14 dykes, and 4 eruptions occurred during 2005–2010 along the Manda Hararo rift segment in Afar (e.g., Wright et al., 2006; Barnie et al., 2016). This was coincident with the eruptions of Jebel at Tair island in 2007 (Xu and Jónsson, 2014) and Alu-Dalafilla in 2008 (Pagli et al., 2012), and followed by the eruptions of Erta Ale in 2010 (Field et al., 2012), Nabro in 2011 (Hamlyn et al., 2014; Goitom et al., 2015), and also increased volcanic activity of the western Gulf of Aden (Ahmed et al., 2016) and of the Zubair Archipelago (Jónsson and Xu, 2015).

DATA AND METHODS

We used seven broadband seismometers in Eritrea, Yemen, and Saudi Arabia (**Figure 1**). A Butterworth band pass filter was applied to the data to only allow frequencies between 1 and 10 Hz for the stations in Eritrea, and 1–8 Hz for the Yemen and Saudi Arabia stations due to a higher level of noise. Earthquakes were manually picked for both P and S waves, and events with a minimum of four arrival times at three stations were located with NonLinLoc, using the Oct-Tree Sampling Algorithm (Lomax et al., 2000). Due to the large distance between stations and earthquakes, the depth of events cannot be reliably constrained, and we therefore fix the depth of earthquakes to 5 km. This is well within the ∼10 km thick crust. We compared locations for depths from 1 to 9 km, which can be seen in **Supplementary Figure 1**. The variance in locations for latitude and longitude were low, showing that constraining the depth to 5 km has minimal overall effect on the location (**Supplementary Table 1**). For our final locations, we used a two-dimensional velocity model based on controlled source experiments (Berckhemer et al., 1975; Egloff et al., 1991). This took into account the shallow low velocity mantle recorded at the rift axis, and the deepening of the Moho

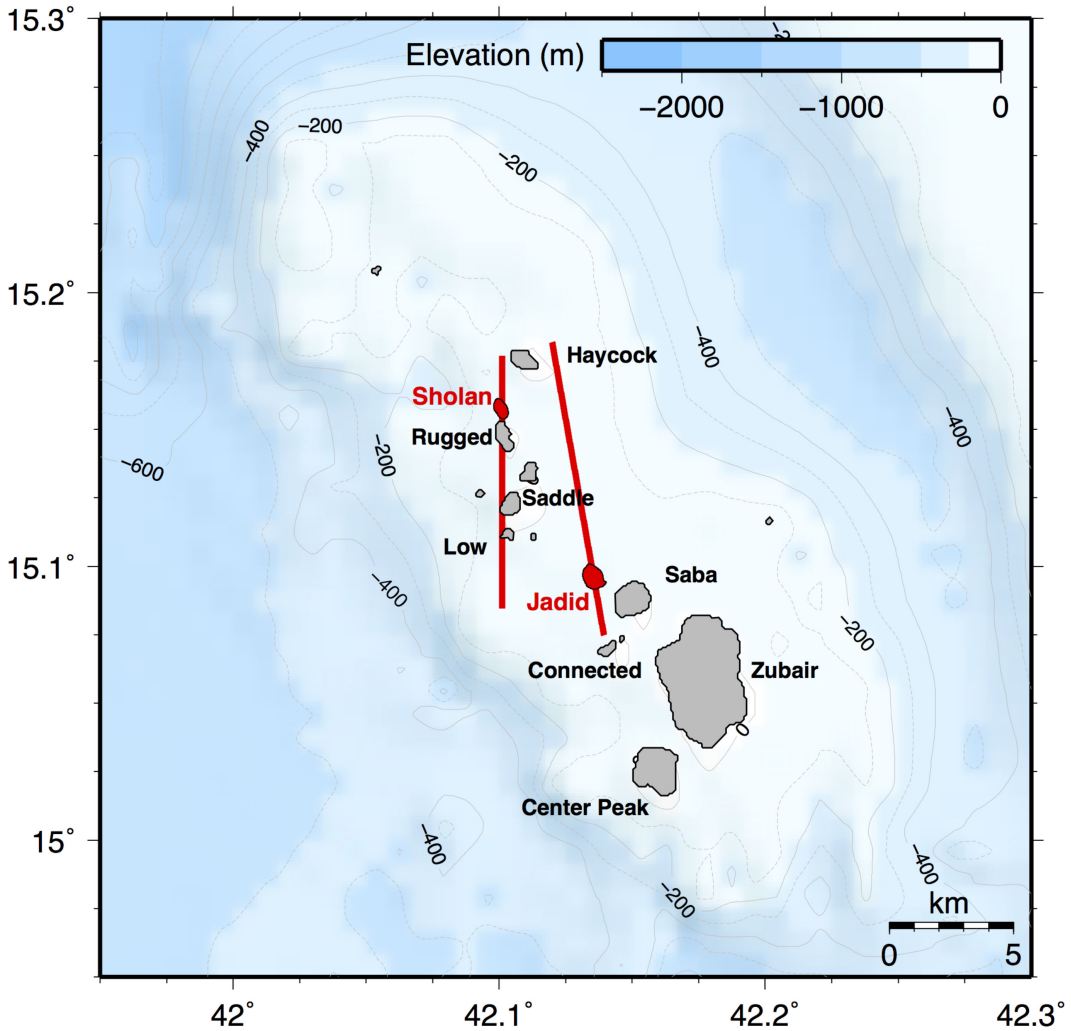

FIGURE 2 | The Zubair archipelago in the Southern Red Sea. Sholan and Jadid Island, erupted in 2011 and 2013, respectively, are shown in red. Proposed dike locations from Xu et al. (2015) are shown as red lines.

along the rift flanks to a maximum depth of 25 km. A constant sediment thickness of 2 km was used across the profile. A variety of velocity models were input into NonLinLoc to see how the overall location of earthquakes varied for different models. A comparison of the locations achieved using the 1D model (**Supplementary Figure 2**) with those achieved with the final 2D model (**Supplementary Figure 3**) used for this study show similar locations for the earthquakes. The 1D model produced more scattered locations, but the relative distribution of earthquakes in both space and time is similar to the extent that our overall interpretation would remain unchanged.

Magnitudes are calculated by measuring the maximum peak-to-peak amplitude and using the local magnitude scale of Illsley-Kemp et al. (2017). Seismic moment release (M_o) is determined using empirical relationships between M_L, m_b, and M_o (e.g., Kanamori, 1977; Hanks and Kanamori, 1979; Scordilis, 2006). Focal mechanisms were further calculated using P-wave polarities and the software FocMec (Snoke, 2003).

RESULTS

Using arrival times from a minimum of 3 and up to 7 seismic stations, we locate 28 individual earthquakes in NonLinLoc in the vicinity of the islands from the 5th December 2011 to the 12th January 2012. Latitude and longitude errors were calculated in NonLinLoc; these are statistical errors based on the probability density function of each earthquake's location (**Supplementary Figure 3**). Five additional earthquakes were removed due to having error bars larger than 5 km, leaving 23 earthquakes that were used for final analysis that define a broadly NW-SE trend (**Figure 3**). Further information on the earthquakes location, errors and statistics can be found in **Supplementary Table 1**. The main seismic events are focused within the Zubair archipelago and occurred during the 12th and 13th December with just two events after this time period (**Figure 4**). The first earthquakes, on the 12th December occur to the north of Sholan island, beneath Haycock island, and then migrate southeast to Saba island with

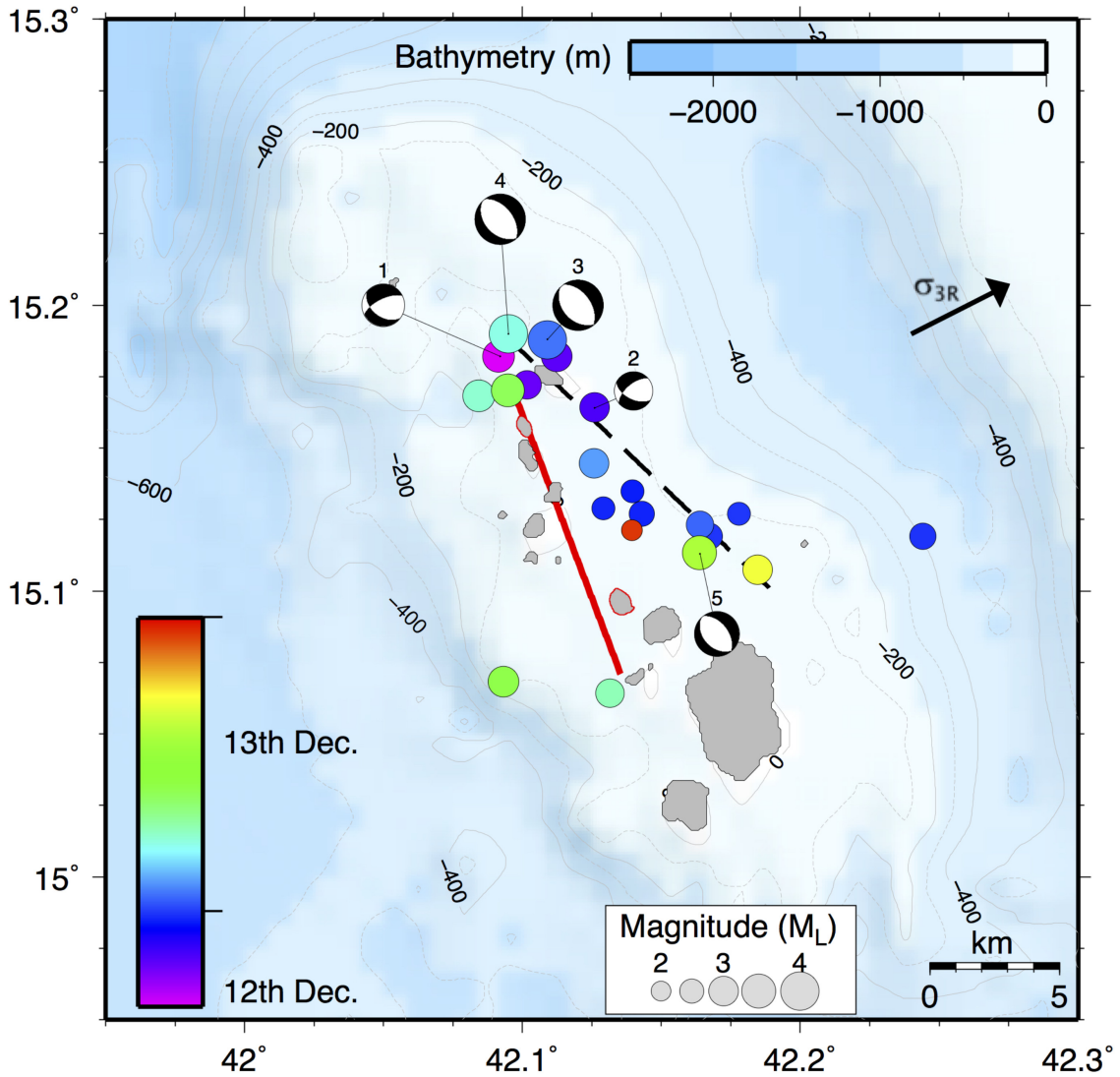

FIGURE 3 | The Sholan seismic sequence with earthquakes colored by time. Focal mechanisms show three normal faulting and two strike-slip faulting events. The black dashed line denotes the inferred dike location taken from earthquake hypocenters only; the red line denotes the final dike location taken from combining ground deformation and earthquake hypocenters.

time (**Figure 3**). The computed errors in horizontal earthquake location are within ±5 km. The PDF scatter clouds produced by NonLinLoc can be seen in **Figure 3**.

The calculated local magnitudes (M_L) vary from 2.1 to 3.9, with the majority of earthquakes ranging from 2.5 to 3.5 (**Figure 4**). No temporal trend in M_L with time can be seen over the 12th–13th December. However, a cluster of low magnitude events is observed at the end of the 12th December. Larger magnitudes are observed north of the island with M_L 2–3 earthquakes further south (**Figure 3**). Cumulative seismic moment calculated over December shows the majority of the energy release occurring on the 12th–13th December, in agreement with the number of events. A gradual increase in energy release to 19×10^{14} Nm is observed over the 12th and 13th December, with little additional energy from the two events on the 16th and 27th (**Figure 4**). Due to quality of data, only five focal mechanisms were adequately constrained (**Table 1** and **Figure 3**). The solutions show a combination of normal fault and strike-slip fault plane solutions (**Figure 3**).

TABLE 1 | Focal plane solutions of five events on 12th–13th December 2011.

ID	DATE	TIME	LAT.	LONG.	MAG.	STRIKE	DIP	RAKE
1	12/12/11	16:59:27	15.182	42.092	3.27	127.4	44.9	−35.3
2	12/12/11	20:45:20	15.164	42.126	2.99	117.0	54.9	−36.3
3	13/12/11	01:22:12	15.188	42.109	3.92	323.5	50.1	−86.1
4	13/12/11	05:01:49	15.190	42.095	3.92	322.1	50.1	−86.1
5	13/12/11	13:02:31	15.113	42.164	3.47	322.1	50.1	−86.7

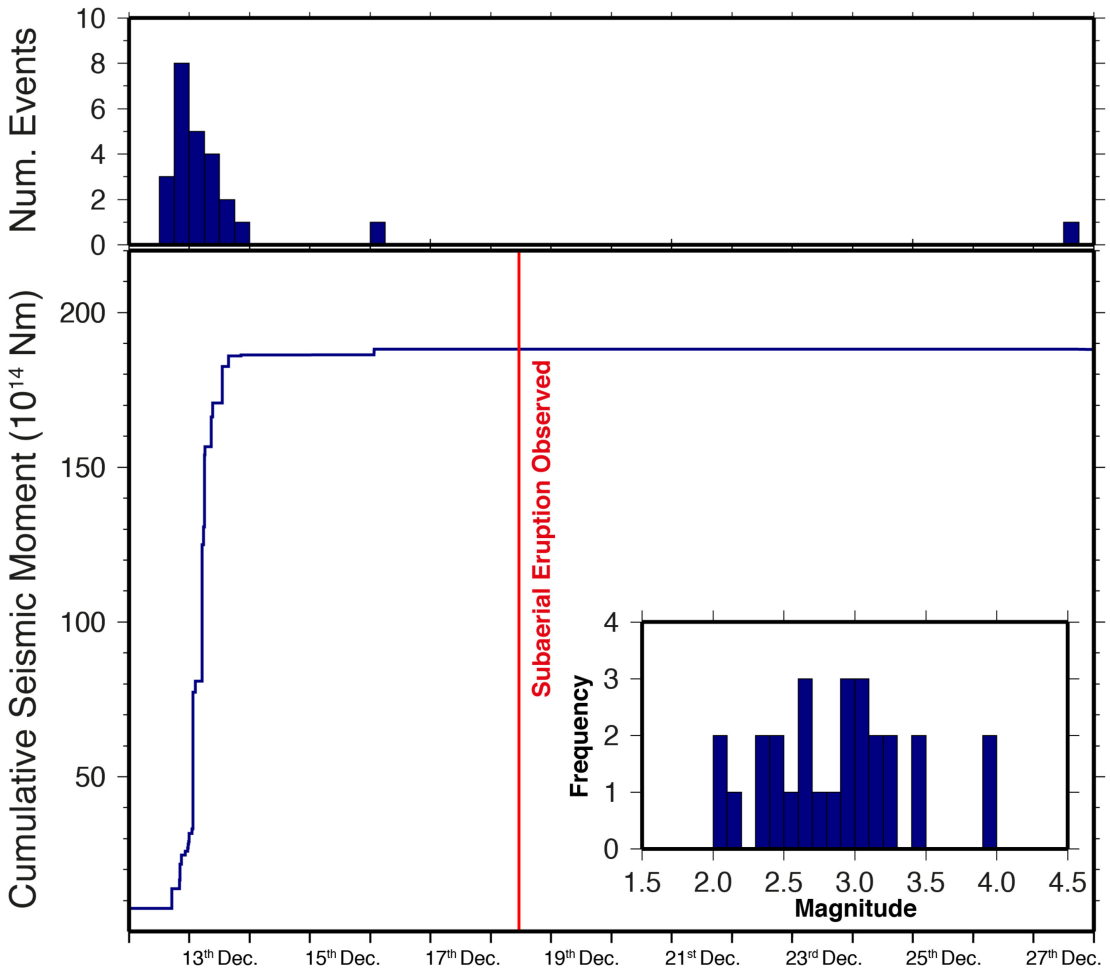

FIGURE 4 | Cumulative seismic moment release and number of events over December 2011 for the Sholan seismic sequence. Inset: histogram displaying the range of magnitudes for events in December 2011. Red line denotes the start of the subaerial eruption.

DISCUSSION

The locations of 23 earthquakes in the Zubair Archipelago shows a clustering of events that follow a NW-SE trend. The variation of event locations with time shows a progression toward the south originating from near Sholan island, with larger magnitude events occurring at either end of the sequence. Earthquakes are commonly induced at the leading edge of a propagating dike due to concentration of extensional stresses (e.g., Roman and Cashman, 2006). We therefore interpret southwards migration of hypocenters on the 12th–13th December as suggesting movement of the dike away from Sholan island. Subsequent earthquakes later on the 13th December, after the initial movement, show hypocenters located at either end of the dike migration pattern. These earthquakes are consistent with the pattern of seismicity at the edges of the final position of the dike once it has reached its full length (**Figure 3**). No spatial or temporal pattern is observed with magnitude during the time frame studied. Using the range of magnitudes calculated, it is suggested that no events under M_L 2 would be recorded. The lack of recorded earthquakes with magnitudes less than 2 is likely due to the distance of the seismic stations from the located hypocenters, which varies from 140 to 300 km. Analysis of seismic moment release shows that the majority of energy release occurred over a 24-h period from the 12th–13th December. This supports results found for the main dike propagation event.

The focal plane solutions show two focal mechanisms (1, 2) which occur on the 12th December in the early stages of dike propagation (**Figure 3**). Both these events display a large component of strike-slip deformation, with p-axes oriented 70° from the regional maximum horizontal compressive stress (σ_{1R}). These two earthquakes are best explained by a model proposed by Roman (2005), which suggests that earthquakes within the walls around a dike growing in width will have p-axes near perpendicular to σ_{1R}. We therefore infer that dike propagation is accompanied by dike inflation, likely behind the propagating tip of the dike. The remaining three focal mechanisms (3, 4, 5) occur on the 13th December, once the dike propagation has largely ceased (**Figure 3**). All three events are located near the tips of the proposed dike location, two near Sholan island and one

near Jadid (**Figure 3**). The location and normal mechanism with extension parallel to the regional minimum compressive stress (σ_3) is consistent with that expected to be caused by induced stress changes near the dike tips, which promotes normal faulting (e.g., Rubin and Gillard, 1998; Roman and Cashman, 2006).

Xu et al. (2015) proposed a north-south orientation of the feeder dike for the Sholan eruption and a NW-SE feeder dike for the 2013 Jadid eruption (**Figure 2**). With the Sholan eruption, their north-south strike was based partly on the short (∼300 m) north-south oriented eruptive fissure and north-south co-diking cracks seen in an optical satellite image from the early phase of the eruption (23 December, 2011). In addition, the modeled ground deformation caused by a N-S striking dike is not inconsistent with the observed ground deformation data. However, the earthquake epicenters found in our study suggests the feeder dike for the Sholan eruption is more likely to strike sub-parallel to the Red Sea rift.

In order to reconcile the observed ground deformation pattern, eruption and ground fracturing locations, and the seismicity we used rectangular dislocations in an elastic halfspace to model the dike opening, and calculated the expected surface deformation from several different possible dike locations. For the models we use a dike depth of 0–5 km, vertical dip, and thickness of 0.5 m. We show the modeled ground deformation patterns from Xu et al. (2015) (**Figure 5A**), from interpretation of the dike position based solely on seismicity (**Figure 5B**), and from a combination of seismicity and the constraints used in Xu et al. (2015; **Figure 5C**). This shows that the calculated deformation pattern on Saba and Zubair islands, where the InSAR observations of Xu et al. (2015) provide key information, is strongly controlled by the location of the SE end of the modeled dike. When the SE end of the dike is NE of Saba and Zubair islands, as constrained from seismicity only (**Figure 5B**), the predicted deformation pattern is inconsistent with the InSAR observations. We thus modified the location of the modeled dike for it to pass through Sholan Island and changed the strike from NW-SE to NNW-SSE such that the SE end is west of Saba and Zubair islands (**Figure 5C**). This modeled dike location agrees with the observed deformation fringes on Saba and Zubair islands, and better reflects the orientation of the seismic cluster. The shift in dike position from that based solely on seismicity, to that based on seismicity and geodesy, are within the error bars of the earthquake locations.

In order to understand the migration of the earthquakes with time, a projection was taken along the length of the inferred dike and compared with the hypocenters of the earthquakes (**Figure 6**). Here we can clearly see that the southward dike propagation occurs between 17:00 on the 12th December and 02:00 on the 13th December, and by varying isotachs (lines of constant speed) we estimate that the dike propagated at a rate of 0.32 ms^{-1}. This compares with a dike propagation event seen at Bárðarbunga in August 2014 which had dike propagation rates of up to 0.83 m/s (Sigmundsson et al., 2015). Propagation rates of 0.2–0.6 km/s was also observed during dike intrusions of both the Krafla and Dabbahu spreading episode (Brandsdottir and Einarsson, 1979; Einarsson, 1991; Keir et al., 2009; Wright et al., 2012). Once the dike had ceased propagating the seismic activity was limited to either end of the dike, near Sholan and Jadid islands.

The cessation of the dike to the south is likely due to the dike reaching a stress barrier such as caused by a topographic load (Urbani et al., 2018), layering in the bedrock (Rivalta et al., 2015), or due to the exhaustion of the magma supply. Topographic loads alter the surrounding stress field, making it difficult for subsurface magma to propagate upslope (Rivalta et al., 2015; Urbani et al., 2018). Similarly, bedrock heterogeneity can result in strong contrasts in elastic parameters, stopping the dike (Rivalta et al., 2015). Due to the eruption occurring several days after the seismic activity, we suggest that the cessation of the dike is not due to magma exhaustion, and instead a result of reaching a stress

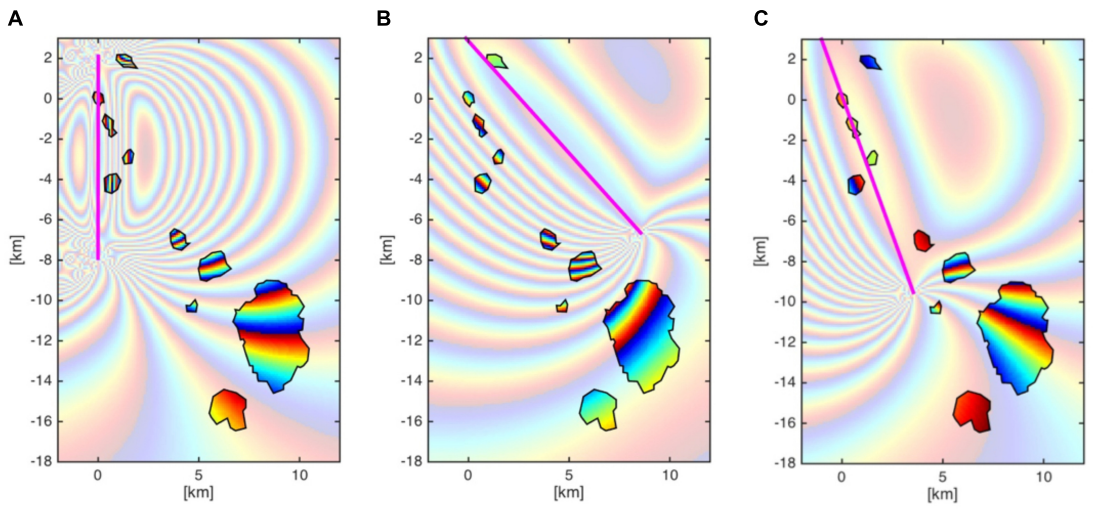

FIGURE 5 | Interferograms produced by modeling the ground deformation pattern using different dike locations. **(A)** Original dike location produced by Xu et al. (2015). **(B)** Dike location interpreted purely from earthquake hypocenters. **(C)** Dike location that satisfies seismicity and geodesy data.

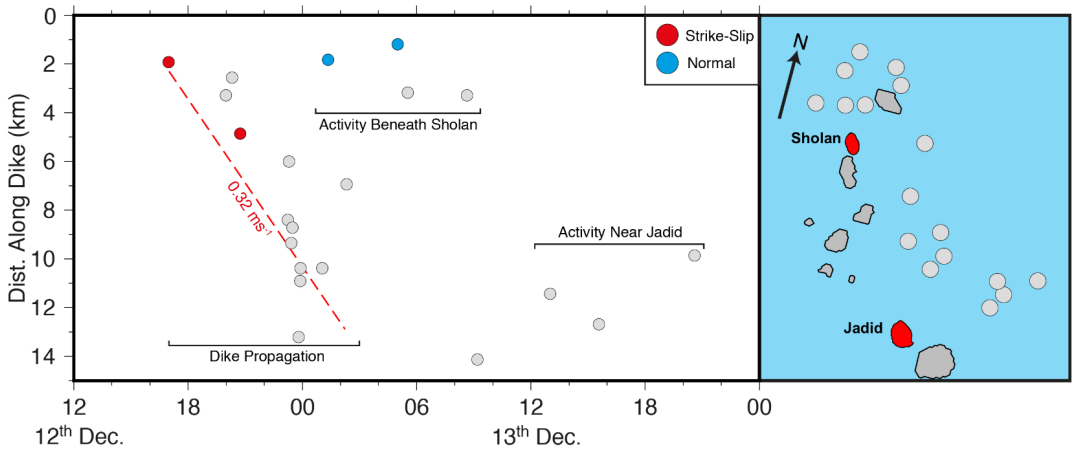

FIGURE 6 | The Sholan seismic sequence projected along the length of the proposed dike. The dike propagation phase is clearly seen with activity at either end of the dike continuing once propagation has ceased. The red dashed line shows the 0.32 ms^{-1} isotach indicating the speed of dike propagation.

barrier, resulting in the eruption occurring at the beginning of the dike.

Little seismicity is recorded after the 13th December, with only one further earthquake recorded prior to the first observation of the subaerial eruption on the 18th December. We suggest that the eruption began as a submarine eruption on the 13th December once the dike had ceased propagating to the south. We interpret this sequence of events using insights from subaerial fissure eruptions in Afar (Belachew et al., 2011; Barnie et al., 2016), where eruptions typically began within hours of the termination of dike propagation. Water depths around Sholan island are less than 100 m, and we therefore suggest that the submarine eruption continued for 5 days, causing the volcanic edifice to increase in height such that on the 18th December it reached the surface and was observed by the Yemeni fishermen. As well as this direct observation of the subaerial eruption, an SO_2 anomaly was also observed on the 19th December. SO_2 is highly soluble in water (Butterfield et al., 2011) and anomalies are typically not observed at submarine eruptions (Barrancos et al., 2012). The lack of an SO_2 anomaly until the eruption became subaerial on the 18th December is therefore consistent with a submarine eruption between the 13th and 18th December. An alternative explanation is that the seismic activity recorded over the 12th and 13th December occurred during an initial dike intrusion that fractured the crust but failed to reach the surface. A second pulse of magma through the already formed conduit, potentially on the 16th December due to an additional earthquake on this date, resulted in the magma erupting at the surface, initiating the submarine eruption and reaching sea level on the 18th December.

There is uncertainty in the nature of the Red Sea ridge between 15.5 and 14.5°N. A lack of magnetic anomalies suggests an absence in seafloor spreading in this region, however, bathymetry data suggest the ridge continues to 14.5°N (Almalki et al., 2016). The revised dike position that we propose is somewhat similar is position and orientation to that constrained for the Jadid eruption (**Figure 2**), and suggests that both dikes were likely intruded along the same rift segment. The modeled dike thicknesses of 0.5 m for Sholan, and 1 m for Jadid are in line with the average 0.5–1.5 m dike thickness most commonly seen at mid-ocean ridges (Qin and Buck, 2008), and also consistent with the hypothesis that they are part of a multi-intrusion spreading episode (Qin and Buck, 2008). The body of evidence suggests that the Zubair archipelago is an active spreading segment with dikes intruding parallel to the trend of the Red Sea, and that the Red Sea ridge is actively accommodating extension at the southern end via spreading episodes similar to those seen at mid-ocean ridges.

CONCLUSION

We analyse a swarm of earthquakes in the Red Sea at 15–15.2°N and 42–42.3°E, associated with a subaerial volcanic eruption starting on the 18th December 2011 that resulted in the formation of Sholan Island. Intense earthquake activity on the 12th December forms a NW-SE trending cluster with the time evolution of seismicity showing a southward migration over a day period. The rapid migration of earthquakes, coupled with earthquakes focused at the lateral tips of the cluster after migration stops strongly suggests the earthquakes are caused by an intrusion that fed the eruption, broadly consistent with surface deformation patterns best modeled using the presence of a dike. The seismicity migration suggests that the dike propagated at speeds of 0.32 ms^{-1} and was approximately 12 km in length. Analysis of focal mechanisms suggests that the seismicity in the early stages of dike propagation was caused by stresses around the expanding dike. Once, propagation had halted seismicity is dominated by normal faulting suggesting dike-induced extension. We interpret dike position and a NNW-SEE orientation based on tested forward models of ground deformation pattern based on both geodetic and the new seismicity data. Observations from other dike intrusions in Afar, coupled with high solubility of SO_2 in water, suggest that a submarine eruption may have begun on the 13th December once the dike had ceased propagating. The intrusion of the dike parallel

to the orientation of the Red Sea suggests seafloor spreading is still active in this region, with the increased seismicity and magmatic activity likely related to a spreading event.

AUTHOR CONTRIBUTIONS

JE conducted seismology analysis, and led the interpretation and writing of the paper. FI-K contributed to seismology analysis, interpretation, and writing the paper. DK contributed to project design, interpretation, and writing the paper. JR contributed to the project design, interpretation, and writing the paper. SJ conducted the InSAR analysis and related modeling, and contributed to interpretation and writing the paper.

FUNDING

FI-K was funded through NERC studentship NE/L002531/1 and a grant to GSNOCS from Roy Franklin O.B.E and the ECLIPSE Program funded by the New Zealand Ministry of Business, Innovation and Employment. DK was supported by NERC grant NE/L013932, and grant number OSR-2015-CRG4-2643 from King Abdullah University of Science and Technology. JE was supported by NERC studentship NE/L002582/1.

ACKNOWLEDGMENTS

We acknowledge the support of Martin Mai (KAUST) in facilitating acquisition of data from Farasan Island from the Saudi Geological Survey, who are also thanked. The remaining data was downloaded from the IRIS-DMC. We thank the reviewers EF and LDS, editor BT, and chief editor Valerio Acocella for constructive reviews.

SUPPLEMENTARY MATERIAL

The Supplementary Material for this article can be found online at: https://www.frontiersin.org/articles/10.3389/feart.2018.00141/full#supplementary-material

REFERENCES

Ahmed, A., Doubre, C., Leroy, S., Kassim, M., Keir, D., Abayazid, A., et al. (2016). Seafloor spreading event in western Gulf of Aden during the November 2010 - March 2011 period captured by regional seismic networks: evidence for diking events and interactions with a nascent transform zone. *Geophys. J. Int.* 205, 1244–1266. doi: 10.1093/gji/ggw068

Almalki, K. A., Betts, P. G., and Ailleres, L. (2016). Incipient seafloor spreading segments: insights from the Red Sea. *Geophys. Res. Lett.* 43, 2709–2715. doi: 10.1002/2016GL068069

Barnie, T. D., Keir, D., Hamling, I., Hofmann, B., Belachew, M., Carn, S., et al. (2016). A multidisciplinary study of the final episode of the Manda Hararo dike sequence, Ethiopia, and implications for trends in volcanism during the rifting cycle. *Geol. Soc. Special Publ.* 420, 149–163. doi: 10.1144/SP420.6

Barrancos, J., Padilla, G., Padron, E., Hernández, P., Calvo, D., Marquez, A., et al. (2012). Estimated CO_2, SO_2 and H_2S emission to the atmosphere from the 2011 El Hierro submarine eruption (Canary Islands) on the basis of helicopter gas surveys. *Geophys. Res. Abstr.* 14:12345.

Belachew, M., Ebinger, C., Cote, D., Keir, D., Rowland, J., Hammond, J., et al. (2011). Comparison of dike intrusions in an incipient seafloor- spreading segment in Afar, Ethiopia: seismicity perspectives. *J. Geophys. Res.* 116:B06405. doi: 10.1029/2010JB007908

Berckhemer, H., Baier, B., Bartlesen, H., Behle, A., Burkhardt, H., Gebrande, H., et al. (1975). "Deep seismic soundings in the Afar region and on the highland of Ethiopia," in *Afar Depression of Ethiopia*, eds A. Pilger and A. R ösler (Stuttgart: Schweizerbart), 89–107.

Bonatti, E. (1985). Punctiform initiation of seafloor spreading in the Red Sea during transition from a continental to an oceanic rift. *Nature* 316, 33–37. doi: 10.1038/316033a0

Bosworth, W., Huchon, P., and McClay, K. (2005). The Red Sea and Gulf of Aden basins. *J. Afr. Earth Sci.* 43, 334–378. doi: 10.1016/j.jafrearsci.2005.07.020

Brandsdottir, B., and Einarsson, P. (1979). Seismic activity associated with the september 1977 deflation of the krafla central volcano in northeastern ice- land. *J. Volcanol. Geothermal Res.* 6, 197–212. doi: 10.1016/0377-0273(79)90001-5

Butterfield, D. A., Nakamura, K. I., Takano, B., Lilley, M. D., Lupton, J. E., Resing, J. A., et al. (2011). High SO_2 flux, sulfur accumulation, and gas fractionation at an erupting submarine volcano. *Geology* 39, 803–806. doi: 10.1130/G31901.1

Carey, R., Soule, S. A., Manga, M., White, J. D., McPhie, J., Wysoczanski, R., et al. (2018). The largest deep-ocean silicic volcanic eruption of the past century. *Sci. Adv.* 4:e1701121. doi: 10.1126/sciadv.1701121

Ebinger, C. J., van Wijk, J., and Keir, D. (2013). The time scales of continental rifting: implications for global processes. *Geol. Soc. Am. Special Papers* 500, 371–396. doi: 10.1130/2013.2500(11)

Egloff, F., Rihm, R., Makris, J., Izzeldin, Y., Bobsien, M., Meier, K., et al. (1991). Contrasting structural styles of the eastern and western margins of the southern Red Sea: the 1988 SONNE experiment. *Tectonophysics* 198, 329–353. doi: 10.1016/0040-1951(91)90159-P

Einarsson, P. (1991). "The Krafla rifting episode 1975–1989," in *Nattura Myvatns (The Nature of Lake Myvatn)*, eds A. Gardarsson and A. Einarsson (Reykjavic: Icelandic Nature Science Society), 97–139.

Field, L., Barnie, T., Blundy, J., Brooker, R. A., Keir, D., Lewi, E., et al. (2012). Integrated field, satellite and petrological observations of the November 2010 eruption of Erta Ale. *Bull. Volc.* 74, 2251–2271. doi: 10.1007/s00445-012-0660-7

Goitom, B., Oppenheimer, C., Hammond, J. O. S., Grandin, R., Barnie, T., Donovan, A., et al. (2015). First recorded eruption of Nabro volcano, Eritrea, 2011. *Bull. Volc.* 77:85. doi: 10.1007/s00445-015-0966-3

Hamlyn, J. E., Keir, D., Wright, T. J., Neuberg, J. W., Goitom, B., Hammond, J. O. S., et al. (2014). Seismicity and subsidence following the 2011 Nabro eruption, Eritrea: insights into the plumbing system of an off-rift volcano. *J. Geophys. Res.* 119, 8267–8282. doi: 10.1002/2014JB011395

Hanks, T. C., and Kanamori, H. (1979). A moment magnitude scale. *J. Geophys. Res.* 84, 2348–2350. doi: 10.1029/JB084iB05p02348

Illsley-Kemp, F., Keir, D., Bull, J. M., Ayele, A., Hammond, J. O., Kendall, J.-M., et al. (2017). Local earthquake magnitude scale and b-value for the Danakil region of northern Afar. *Bull. Seis. Soc. Am.* 107, 521–531. doi: 10.1785/0120150253

Jónsson, S., and Xu, W. (2015). *Volcanic Eruptions in the Southern Red Sea During 2007-2013. The Red Sea*. Berlin: Springer, 175–186. doi: 10.1007/978-3-662-45201-1_10

Kanamori, H. (1977). The energy release in great earthquakes. *J. Geophys. Res.* 82, 2981–2987. doi: 10.1029/JB082i020p02981

Keir, D., Hamling, I. J., Ayele, A., Calais, E., Ebinger, C., Wright, T. J., et al. (2009). Evidence for focused magmatic accretion at segment centers from lateral dike injections captured beneath the Red Sea rift in Afar. *Geology* 37, 59–62. doi: 10.1130/G25147A.1

Le Pichon, X. T., and Gaulier, J.-M. (1988). The rotation of Arabia and the levant fault system. *Tectonophysics* 153, 271–294. doi: 10.1016/0040-1951(88)90020-0

Lomax, A., Virieux, J., Volant, P., and Berge-Thierry, C. (2000). "Probabilistic earth- quake location in 3D and layered models," in *Advances in Seismic Event*

Location, eds C. H. Thurber and N. Rabinowitz (Berlin: Springer), 101–134. doi: 10.1007/978-94-015-9536-0_5

McClusky, S., Reilinger, R., Ogubazghi, G., Amleson, A., Healeb, B., Vernant, P., et al. (2010). Kinematics of the southern Red Sea-Afar Triple Junction and implications for plate dynamics. *Geophys. Res. Lett.* 37:L05301. doi: 10.1029/2009GL041127

Pagli, C., Mazzarini, F., Keir, D., Rivalta, E., and Rooney, T. O. (2015). Introduction: anatomy of rifting: tectonics and magmatism in continental rifts, oceanic spreading centers, and transforms. *Geosphere* 11, 1256–1261. doi: 10.1130/GES01082.1

Pagli, C., Wright, T. J., Ebinger, C. J., Yun, S.-H., Cann, J. R., Barnie, T., et al. (2012). Shallow axial magma chamber at the slow-spreading Erta Ale Ridge. *Nat. Geosci.* 5, 284–288. doi: 10.1038/ngeo1414

Qin, R., and Buck, W. R. (2008). Why meter-wide dikes at oceanic spreading centres? *Earth Planet. Sci. Lett.* 265, 466–474. doi: 10.1016/j.epsl.2007.10.044

Rivalta, E., Taisne, B., Bunger, A., and Katz, R. (2015). A review of mechanical models of dike propagation: schools of thought, results and future directions. *Tectonophysics* 638, 1–42. doi: 10.1016/j.tecto.2014.10.003

Roman, D. C. (2005). Numerical models of volcanotectonic earthquake triggering on non-ideally oriented faults. *Geophys. Res. Lett.* 32:4. doi: 10.1029/2004GL021549

Roman, D. C., and Cashman, K. V. (2006). The origin of volcano-tectonic earthquake swarms. *Geology* 34, 457–460. doi: 10.1130/G22269.1

Rubin, A. M., and Gillard, D. (1998). Dike-induced earthquakes: theoretical considerations. *J. Geophys. Res.* 103, 10017–10030. doi: 10.1029/97JB03514

Ruch, J., Wang, T., Xu, W., Hensch, M., and Jónsson, S. (2016). Oblique rift opening revealed by reoccurring magma injection in central Iceland. *Nat. Commun.* 7:12352. doi: 10.1038/ncomms12352

Schettino, A., Macchiavelli, C., Pierantoni, P. P., Zanoni, D., and Rasul, N. (2016). Recent kinematics of the tectonic plates surrounding the Red Sea and Gulf of Aden. *Geophys. J. Int.* 207, 457–480. doi: 10.1093/gji/ggw280

Scordilis, E. M. (2006). Empirical global relations converting Ms and mb to moment magnitude. *J. Seismol.* 10, 225–236. doi: 10.1007/s10950-006-9012-4

Sigmundsson, F., Hooper, A., Hreinsdóttir, S., Vogfjörd, K. S., Ófeigsson, B. G., Heimisson, E. R., et al. (2015). Segmented lateral dyke growth in a rifting event at Bararbunga volcanic system. *Icel. Nat.* 517, 191–195. doi: 10.1038/nature14111

Snoke, J. A. (2003). FOCMEC: focal mechanism determinations. *Int. Handb. Earthq. Eng. Seismol.* 85, 1629–1630. doi: 10.1016/S0074-6142(03)80291-7

Soule, S. A., Fornari, D. J., Perfit, M. R., and Rubin, K. H. (2007). New insights into mid-ocean ridge volcanic processes from the 2005-2006 eruption of the East Pacific Rise, 9 46 N-9 56 N. *Geology* 35, 1079–1082. doi: 10.1130/G23924A.1

Urbani, S., Acocella, V., Rivalta, E., and Corbi, F. (2018). Propagation and arrest of dikes under topography: models applied to the 2014 Bardarbunga (Iceland) rifting event. *Geophys. Res. Lett.* 44, 6692–6701. doi: 10.1002/2017GL073130

Wilcock, W. S., Tolstoy, M., Waldhauser, F., Garcia, C., Tan, Y. J., Bohnenstiehl, D. R., et al. (2016). Seismic constraints on caldera dynamics from the 2015 axial seamount eruption. *Science* 354, 1395–1399. doi: 10.1126/science.aah5563

Wright, T., Ebinger, C., Biggs, J., Ayele, A., Yirgu, G., Keir, D., et al. (2006). Magma-maintained rift segmentation at continental rupture in the 2005 Afar dyking episode. *Nature* 442, 291–294. doi: 10.1038/nature04978

Wright, T. J., Sigmundsson, F., Pagli, C., Belachew, M., Hamling, I. J., Brandsdóttir, B., et al. (2012). Geophysical constraints on the dynamics of spreading centres from rifting episodes on land. *Nat. Geosci.* 5, 242–250. doi: 10.1038/ngeo1428

Xu, W., and Jónsson, S. (2014). The 2007-8 volcanic eruption on Jebel at Tair island (Red Sea), observed by satellite radar and optical images. *Bull. Volc.* 76, 795–808. doi: 10.1007/s00445-014-0795-9

Xu, W., Ruch, J., and Jónsson, S. (2015). Birth of two volcanic islands in the southern Red Sea. *Nat. Commun.* 6:7104. doi: 10.1038/ncomms8104

Conflict of Interest Statement: The authors declare that the research was conducted in the absence of any commercial or financial relationships that could be construed as a potential conflict of interest.

Copyright © 2018 Eyles, Illsley-Kemp, Keir, Ruch and Jónsson. This is an open-access article distributed under the terms of the Creative Commons Attribution License (CC BY). The use, distribution or reproduction in other forums is permitted, provided the original author(s) and the copyright owner(s) are credited and that the original publication in this journal is cited, in accordance with accepted academic practice. No use, distribution or reproduction is permitted which does not comply with these terms.